Re-examination of Physical Models in the Temperature Range 300 K – 700 K

Andreas Schenk [1]

Technical Report No. 99/01

[1] **This work was supported by the German Bundesministerium für Bildung und Forschung under contract 01 M 3034 A. The authors are responsible for the contents of this publication.**

Abstract

In the PARASITICS project physical models used in device simulation are to be verified for the temperature range 300 K – 700 K (lattice temperature) by comparison between simulation and electrical characterization of suitable test structures. A pre-evaluation of the decisive models in DESSIS$_{-\mathrm{ISE}}$ showed good agreement with existing experimental data up to 500 K and normal physical behavior up to 1000 K. The mobility model of Schenk [1] was fine-tuned by means of a careful analysis of all existing data on the temperature dependence of the mobility. Drift velocity saturation is now perfectly reproduced for both electrons and holes, provided the energy relaxation times are given the values $\tau_{E,n} = 0.75$ ps, $\tau_{E,p} = 0.17$ ps in the simulation. A complete device analysis of DIODE24_BL from MOD_B_BOSCH based on doping profiles by ST and measured IV-characteristics in the temperature range 300 K – 700 K with the device simulator DESSIS$_{-\mathrm{ISE}}$ produced the following results: At all temperatures the forward-bias range is dominated by SRH recombination up to a current of 1×10^{-5} A, and by trap-assisted Auger (TAA) recombination above. The latter is the sum of temperature-dependent contributions from p^+-region, n-region, and buried layer. The measured temperature dependence of the high-injection range of the IV-curves is possibly due to the TAA coefficients, which could not be worked out since DESSIS$_{-\mathrm{ISE}}$ did not converge there. All alternative possibilities - band gap, carrier statistics, BGN model, surface recombination, and band-to-band Auger recombination could be systematically ruled out. The temperature dependence of the reverse-bias IV-curves results from the changing contributions of p^+-region, n-region, and buried layer, respectively, to the total SRH generation rate. Using the fit parameters of the lifetime models in DESSIS$_{-\mathrm{ISE}}$, reasonable overall agreement was achieved without any hypothetical temperature dependence of the minority carrier lifetimes. A good match to the measured breakdown voltages was obtained for all temperatures with a modification of the vanOverstraeten model of the impact ionization coefficient of the form

$$\alpha = const\,\gamma \frac{E_g(300\,K)}{E_g(T)} \exp\left[-\frac{\gamma b}{F}\frac{E_g(T)}{E_g(300\,K)}\right] .$$

which assumes the temperature-dependent band gap to be the threshold energy.

Zusammenfassung

Ziel des Projekts ist die Verifizierung der physikalischen Modelle im Temperaturbereich 300 K – 700 K (Gittertemperatur) durch Vergleich von Simulation und elektrischer Charakterisierung geeigneter Teststrukturen. Dazu wurden im Vorfeld die wichtigsten Modelle in DESSIS$_{-\mathrm{ISE}}$ auf ihr Verhalten bis 1000 K Gittertemperatur hin untersucht. Alle Modelle zeigten gute Übereinstimmung mit vorhandenen Messergebnissen (bis max. 500 K) sowie normales physikalisches Verhalten bis 1000 K.

Ein Schwerpunkt des Projekts ist der Test des physik-basierten Silizium Bulk-Beweglichkeitsmodells von Schenk [1] bei hohen Temperaturen. Zur Vorbereitung der Hochtemperatur-Hall-Messungen wurde das Modell mit sämtlichen vorhandenen Messungen der Abhängigkeit von Gitter- und Ladungsträgertemperatur verglichen. Die existierenden Daten über die Sättigung der Driftgeschwindigkeit (bis max. 370 K) wurden benutzt, um eine Feinanpassung der funktionalen Form zu erhalten, nach der sich perfekte Sättigung der Driftgeschwindigkeit für Elektronen und Löcher ergibt. Die optimalen Energie-Relaxationszeiten für die beste Anpassung an experimentelle Daten wurden ermittelt ($\tau_{E,n} = 0.75\,\mathrm{ps}$, $\tau_{E,p} = 0.17\,\mathrm{ps}$). Die benötigten Hall-Faktoren bis 700 K für alle relevanten Dotierungen der im Projekt gegebenen Teststrukturen wurden bereitgestellt.

Eine vollständige Bauelemente-Analyse der DIODE24_BL von MOD_B_BOSCH (laterale pPlus/nWell smart-power Diode) wurde basierend auf Dotierprofilen von ST und Kennlinien-Messungen im Temperaturbereich 300 K – 700 K mit dem Bauelemente-Simulator DESSIS$_{-\mathrm{ISE}}$ durchgeführt. Wegen der grossen Komplexität dieses Bauelements (laterale pn-Übergänge, Durchbruch an der Si-SiO_2-Grenzfläche, hochdotierte vergrabene Schicht) sind die Ergebnisse mit gewissen Unsicherheiten behaftet. Sie setzen insbesondere voraus, dass die lateralen Dotierprofile korrekt sind und der Avalanche-Durchbruch nicht wesentlich durch die Grenzfläche beeinflusst wird.

Die Analyse der Vorwärts-Kennlinien erbrachte folgende Resultate: SRH-Rekombination dominiert bis zu einer Stromstärke von 1×10^{-5} A im gesamten Temperaturbereich, wobei der Beitrag des n-Gebiets mit steigender Temperatur zunimmt. Oberhalb 1×10^{-5} A ist trap-assistierte Auger-Rekombination (TAA) der einzig wichtige Rekombinationsmechanismus, wobei in Abängigkeit von der Temperatur alle drei Gebiete – p^+-Gebiet, n-Gebiet und vergrabene Schicht – Anteile liefern. Band-Band-Auger-Rekombination würde um drei Grössenordnungen zu grosse Auger-Koeffizienten erfordern. Die starke Temperatur-Abhängigkeit der Kennlinien im Hochinjektionsbereich könnte nur über die TAA-Koeffizienten erklärt werden. Eine entsprechende Anpassung konnte jedoch nicht erfolgen, weil DESSIS$_{-\mathrm{ISE}}$ in diesem Bereich nicht konvergierte. Sämtliche alternativen Möglichkeiten für den gemessenen Temperatur-Einfluss – Energielücke, Ladungsträgerstatistik, BGN-Modell und Oberflächen-Rekombination – konnten systematisch ausgeschlossen werden. Die Dominanz der TAA-Rekombination resultiert aus der Tatsache, dass die Implantation der vergrabenen Schicht ein voluminöses Gebiet mit sowohl hoher Elektronendichte (was einen Auger-Prozess begünstigt) als auch mit hoher Trap-Dichte erzeugt (was einen SRH-Prozess begünstigt). Die Vorwärts-Kennlinien sind demnach wesentlich durch Eigenschaften der vergrabenen Schicht bestimmt.

Die Temperatur-Abhängigkeit der Sperrströme ist durch die wechselnden

Beiträge der einzelnen Gebiete – p^+n-Übergang, n-Gebiet und vergrabene Schicht – zur totalen SRH-Rate bestimmt. Eine genaue Anpassung würde die Kenntnis der Lebensdauerprofile im gesamten Bauelement erfordern. Jedoch gelingt bereits mit sinnvollen Variationen der Lebensdauer-Modellparameter eine gute Simulation der Sperrströme, ohne jegliche (hypothetische) Temperatur-Abhängigkeit der Minoritätsladungsträgerlebensdauern. Insbesondere kann die charakteristische Änderung der Form der Sperr-Kennlinien zu einem “rechteckigen" Verlauf ab etwa 350 K erklärt werden. Die Durchbruchspannungen bei hohen Temperaturen können zwanglos mit dem Lokalfeldmodell der Stossionisationsrate simuliert werden, wenn für die Schwellenenergie die temperaturabhängige Energielücke benutzt wird. Diese wurde ins vanOverstraeten-Modell implementiert, so dass sich

$$\alpha = const\,\gamma \frac{E_g(300\,K)}{E_g(T)} \exp\left[-\frac{\gamma b}{F}\frac{E_g(T)}{E_g(300\,K)}\right] .$$

für den Stossionisationskoeffizienten ergibt. Die gute Übereinstimmung mit den gemessenen Durchbruchspannungen ist ein starkes Indiz für die Richtigkeit der T-Abhängigkeit der Energielücke bis 700 K. Die gemessenen Durchbrüche sind jedoch weicher als die simulierten, was evtl. mit dem lateralen Dotierprofil zu tun hat.

1 Introduction: DESSIS physical models at high ambient temperatures

Transport models have been verified in the literature up to 500 K at the most. The following figures contain extrapolations up to 1000 K obtained from simulations with the implemented models in DESSIS$_{-\mathrm{ISE}}$. Only those physical models that can be expected to yield a significant temperature effect were selected. There is a striking uncertainty in the temperature range between 500 K and 1000 K. The combination of measurements at high temperatures with device simulation of suitable test structures can help in reducing this uncertainty.

Fig. 1 shows the temperature dependence of the indirect band gap of silicon compared to experimental data [2], (p. 17). Such a temperature dependence results from a change of the dominant phonon frequencies (electron energies are renormalized by the electron-phonon coupling) and the static expansion of the crystal. The purely phenomenological $E_g(T_L)$ model in DESSIS$_{-\mathrm{ISE}}$ yields both a good fit in the experimentally covered range and a “normal” behavior at very high temperatures. The dashed curve in Fig. 1 indicates another possible course. Knowing $E_g(T_L)$ is crucial for other transport parameters like the intrinsic density, the band-to-band tunneling rate, the threshold energy of impact ionization, and others.

Fig. 2 shows the temperature dependence of the impact ionization coefficient for electrons in Lackner’s model [2], (p. 99). Since the critical field of the Chynoweth formula is proportional to the total phonon scattering rate, the temperature effect has been traced back to a phonon occupation factor of the form $2f_B + 1 = \coth(\hbar\omega_{op}/2k_BT_L)$. With rising lattice temperature, electrons are more frequently scattered at optical phonons with energy $\hbar\omega_{op}$ and hence need a longer distance to trigger the impact ionization process. The threshold energy E_i is roughly

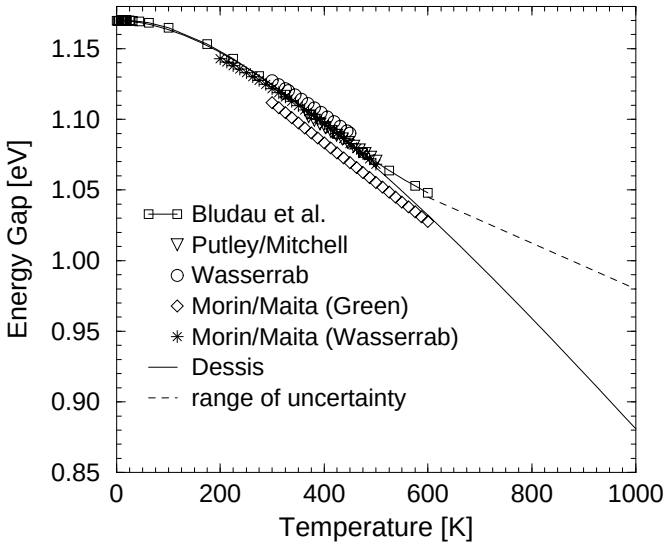

Figure 1: Temperature dependence of the indirect band gap in silicon. See the DESSIS$_{-\mathrm{ISE}}$ manual for the $E_g(T_L)$ formula.

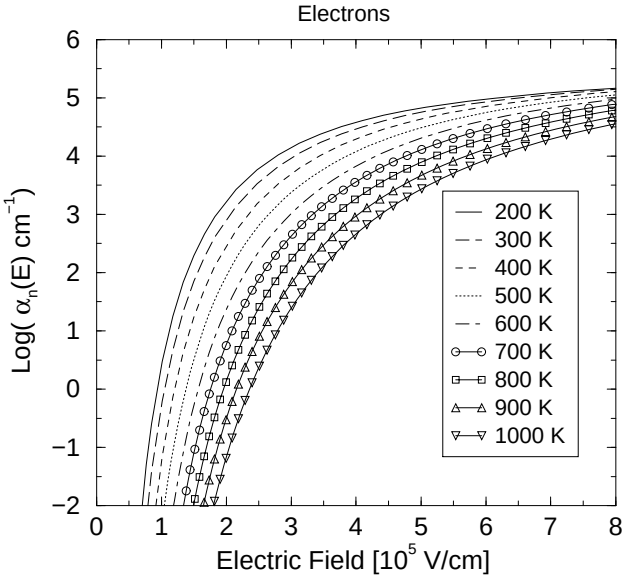

Figure 2: Impact ionization coefficient for electrons as function of electric field as it turns out from Lackner's model.

given by the band gap and, therefore, should exhibit the (strong) temperature dependence of the latter. This will be detailed below.

The drift velocity saturation for electrons at different lattice temperatures from Canali's model [2], (p. 65) is shown in Fig. 3. It decreases with rising temperature at a

fixed field strength in the Ohmic regime. In the saturation range the spacing between different curves becomes narrower with increasing temperature. This indicates that the relative decrease of the saturation velocity declines at higher temperatures.

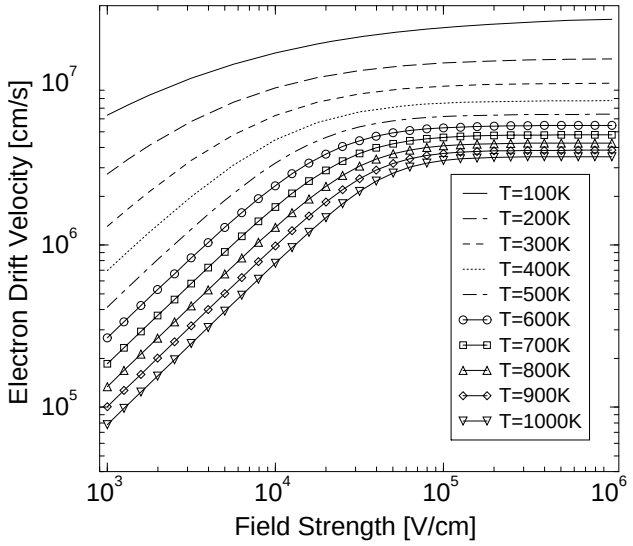

Figure 3: Electron drift velocity as function of electric field for different lattice temperatures as it turns out from Canali's model.

In Fig. 4 the bulk mobility of Schenk [2], (p. 127) is compared with the DESSIS$_{-\mathrm{ISE}}$ default model and experimental data in the entire temperature range up to 1000 K. Despite the good coincidence, the range between 500 K and 1000 K requires further investigations.

The physics-based Schenk mobility model allows conclusions about the scattering of hot carriers in doped (bulk) silicon. Fig. 5 depicts the electron mobility as function of the electric field at different doping levels. In the 300 K case an interesting behavior is observed which can be explained as follows: When the carrier temperature reaches a certain value, the Coulomb scattering at ionized dopants becomes less important and the mobility increases. Further carrier heating, however, immediately leads to the common saturation effect due to the balance between energy gain by the electric field and energy loss by emission of optical phonons. At the highest doping concentrations, the increase of the mobility only sets in after velocity saturation had already started to be effective. The latter behavior was only found for electrons but not for holes. In the right part of Fig. 5 results for 700 K are shown on the same scale. One observes that at high lattice temperatures the described effects do not occur because the saturation mechanism dominates.

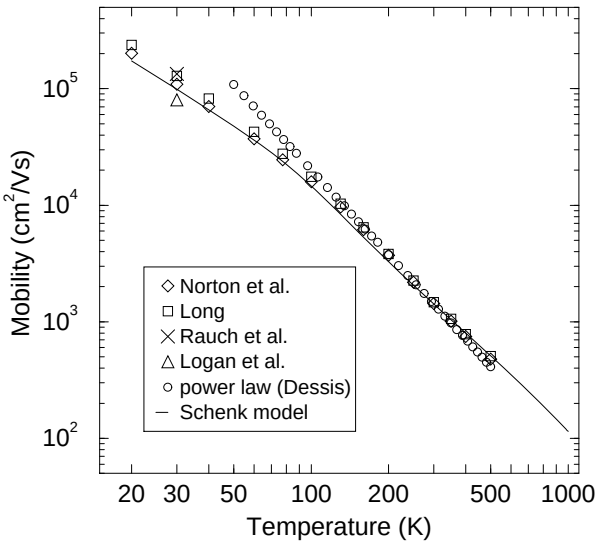

Figure 4: Electron bulk mobility as function of lattice temperature as it turns out from Schenk's model compared to experimental data and the DESSIS$_{-\mathrm{ISE}}$ default model.

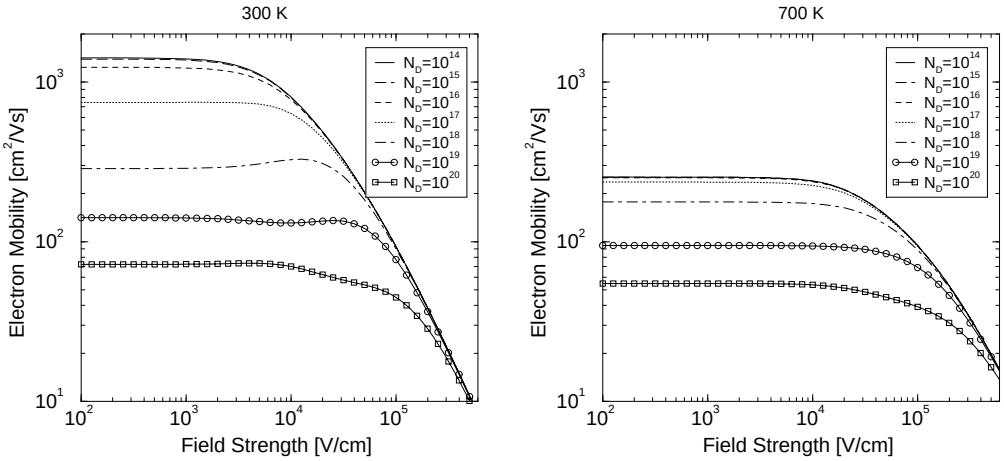

Figure 5: Electron bulk mobility as function of electric field for different doping concentrations as it turns out from Schenk's model. Left: $T_L = 300K$, right: $T_L = 700K$

2 Drift velocity saturation in Schenk's bulk mobility model

2.1 Simulation of n-type resistor

It is commonly believed that the drift velocity in bulk silicon perfectly saturates both in the case of electrons and holes, if the local electric field exceeds 2×10^5 V/cm. The

bulk mobility model as published in Ref. [1] was slightly modified to reproduce this perfect velocity saturation. For this, the integral factor $I_{ac}(T_c) = 2(1 + 12\alpha k_B T_c)$ in the expressions describing phonon scattering had to be changed to $2\sqrt{1 + 24\alpha k_B T_c}$, which obviously does not affect at all the behavior in the Ohmic regime (low T_c). The consequence of this modification is that in the high-T_c regime ($24\alpha k_B T_c \gg 1$) the phonon-limited mobility becomes $\sim T_c^{-1}$. On the other hand, the carrier temperature T_c essentially becomes proportional to the field F (instead of F$\sim T_c^2$ at low T_c), and hence the drift velocity automatically saturates. The modification is not justified by any rigid derivation, but could be attributed to the over-simplified band structure model that had to be used in the calculation of the analytical mobility.

The test device chosen for the comparison with available experimental data is sketched in Fig. 6. A $11\,\mu m$ long 1D resistor with Ohmic contact regions and a low doping level of $N_{dop} = 10^{15}\,\mathrm{cm}^{-3}$ in the inner region of length $l = 10\,\mu m$ was biased up to $200\,V$. The Ohmic regions are indispensable to get DESSIS$_{-\mathrm{ISE}}$ converged in the “Hydrodynamic" mode. Drift velocity and electric field were extracted either

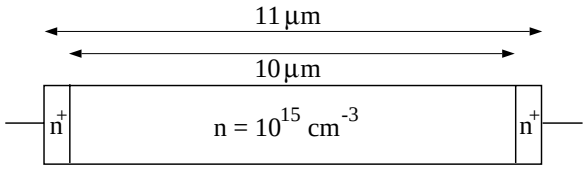

Figure 6: Simulated 1D n-type resistor with Ohmic contacts ($n^+ = 10^{20}\,\mathrm{cm}^{-3}$). Data where either extracted from an inner point (“local”) where field and density are sufficiently constant, or taking average values $v_D(F) \sim j/(10^{15}\,\mathrm{cm}^{-3})$, $F = V_{bias}/l$ (“terminal”).

locally, i.e. at an inner point where field and density were homogeneous (labeled “local”), or from the clamping quantities, i.e. $F = V_{bias}/l$, $v_D(F) \sim j/N_{dop}$ (labeled “terminal”). The latter method which is closer to the measurement improved the situation in the Ohmic regime, where the model parameters were adjusted to independent experimental data (compare Fig. 4). Under increasing bias, carriers are injected from the electrodes into the inner region and the density exceeds the local doping level. Therefore, a third method was applied where the carrier densities averaged over the inner region were used instead of N_{dop}. In the high-field regime this method gave identical results to the first method, hence those results are not shown here.

Fig. 7 containes three curves in a semi-logarithmic plot. The green curve is the result from the local extraction method when only default parameters are used, i.e. in particular the nonparabolicity parameter $\alpha_n = 0.5\,\mathrm{eV}^{-1}$ and the energy relaxation time $\tau_{E,n} = 0.45\,\mathrm{ps}$. The latter is not a parameter of the mobility model, however, it has an outstanding impact since it determines for a given bias the carrier temperatur resulting from the self-consistent solution of energy balance and continuity equations. Although it is possible to depress the saturation velocity to 1×10^7 V/cm by increasing α_n to a large value of $0.9\,\mathrm{eV}^{-1}$ or so, this procedure was not considered to be reasonable. The sensitivity of the mobility model to the local carrier temperature rather demands for an adjustment of the energy relaxation time $\tau_{E,n}$. When the latter is increased to $0.75\,\mathrm{ps}$, Canali’s data [3] can be reproduced very well

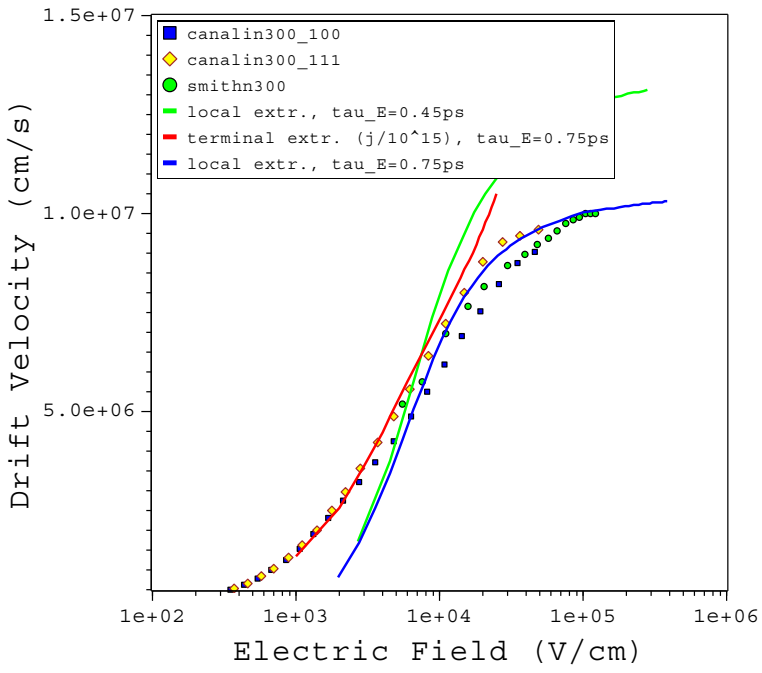

Figure 7: Electron drift velocity at room temperature. Experimental data points are for different substrate orientations ($\langle 100 \rangle$ or $\langle 111 \rangle$).

(blue curve). The red curve represents the result of the terminal extraction method which yields a perfect fit in the Ohmic regime (this has to be so, since deformation potentials and phonon energies had been fixed to reproduce the Ohmic mobility). The above mentioned effect of carrier injection becomes visible at approximately 4×10^3 V/cm. If the third method is applied, the red curve merges with the blue one at about 1×10^4 V/cm.

From this exercice we draw the conclusion that the only change to be made in the set of parameters is the choice $\tau_{E,n} = 0.75\,\mathrm{ps}$.

2.2 Simulation of p-type resistor

Exchanging *n* by *p* in Fig. 6 defines the p-type resistor used to optimize the parameters for the hole drift velocity. In Fig. 8 the green curve again represents the result obtained with default values. In order to match the data of Smith, α_p would have to be further reduced. However, the low value $\alpha_p = 0.15\,\mathrm{eV}^{-1}$ had already been a concession to a reasonable fit of the drift velocity in Ref. [1]. The best fit of the hole DOS was found with $\alpha_p = 0.5\,\mathrm{eV}^{-1}$. Therefore, we better leave the nonparabolicity parameter untouched and adjust the energy relaxation time $\tau_{E,p}$ as above (blue and black curves). A reasonable agreement with the scattering experimental data is found using $\tau_{E,p} = 0.17\,\mathrm{ps}$ or larger (up to 0.20 ps). It is impossible to reproduce the sharp saturation behavior found by Smith [4]. As in the case of electrons, the terminal extraction method gives a perfect fit in the Ohmic regime.

We conclude that $\alpha_p = 0.5\,\mathrm{eV}^{-1}$ and $\tau_{E,p} = 0.17\,\mathrm{ps}$ are the best choice and hence

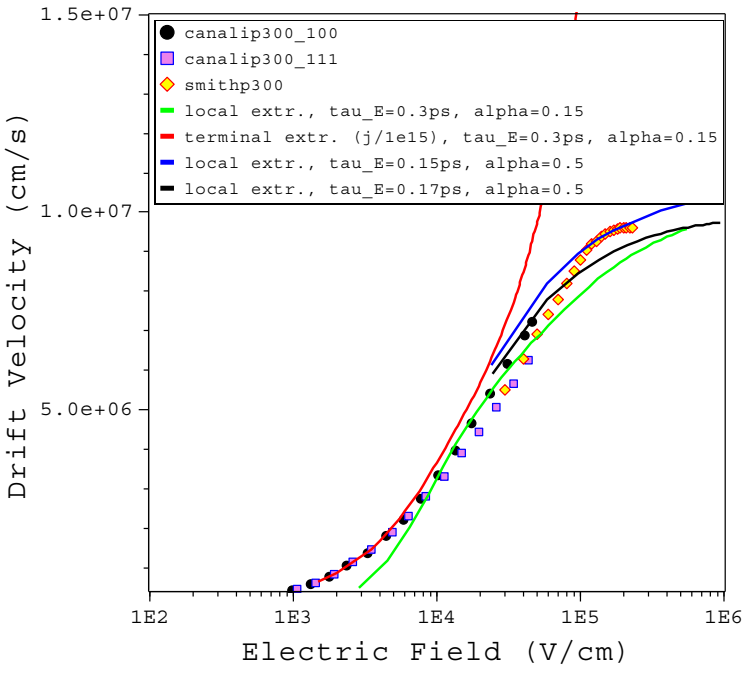

Figure 8: Hole drift velocity at room temperature.

will be used in the high-temperature investigations.

2.3 Comparison with published data on ambient temperature dependence

There exist a few published data for ambient temperatures different from room temperature. In Figs. 9 and 10 we show the drift velocities for 245 K and 370 K in comparison to data by Canali *et al* [3]. In the case of electrons the agreement is equally good using the same parameters as for room temperature. In the case of holes the 370 K curve fits very well with the same parameters that have been found for 300 K, whereas for the lower temperature a larger misfit occurs. Increasing the energy relaxation time would improve the situation, however it seems to be more likely that the misfit is related to the use of an effective hole mass which strongly depends on temperature in DESSIS$_{-\mathrm{ISE}}$. We already argued in Ref. [2], (p. 163) that the T_L-dependence of the hole DOS mass should not be used for transport calculations.

3 DIODE24_BL from MOD_B_BOSCH

3.1 2D default simulation

A cross section of the planar diode DIODE24_BL (pPlus/nWell) together with a zoom into the critical region are shown in Fig. 11. Avalanche breakdown occurs in small areas on both sides of the p^+n junction just below the Si-SiO_2 interface.

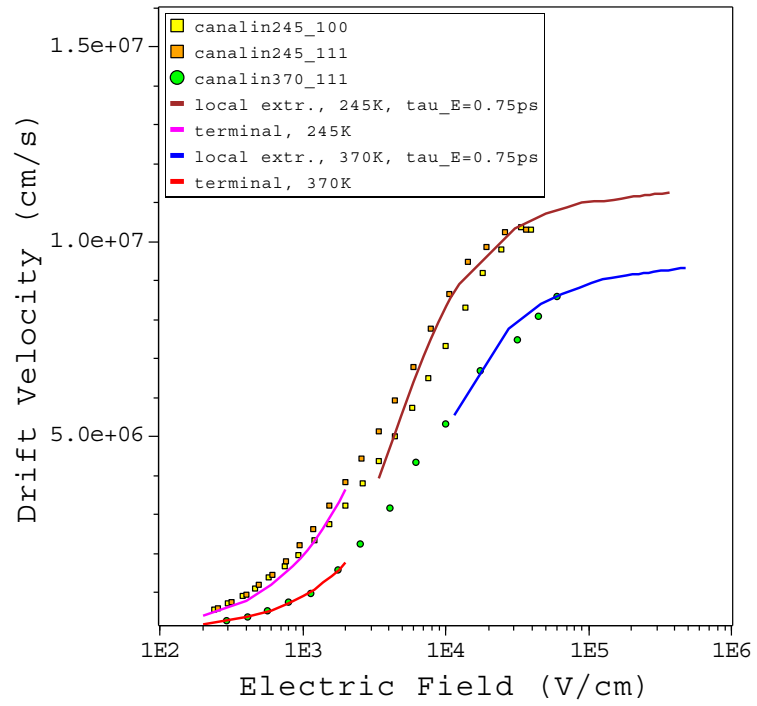

Figure 9: Electron drift velocity versus electric field for different lattice temperatures.

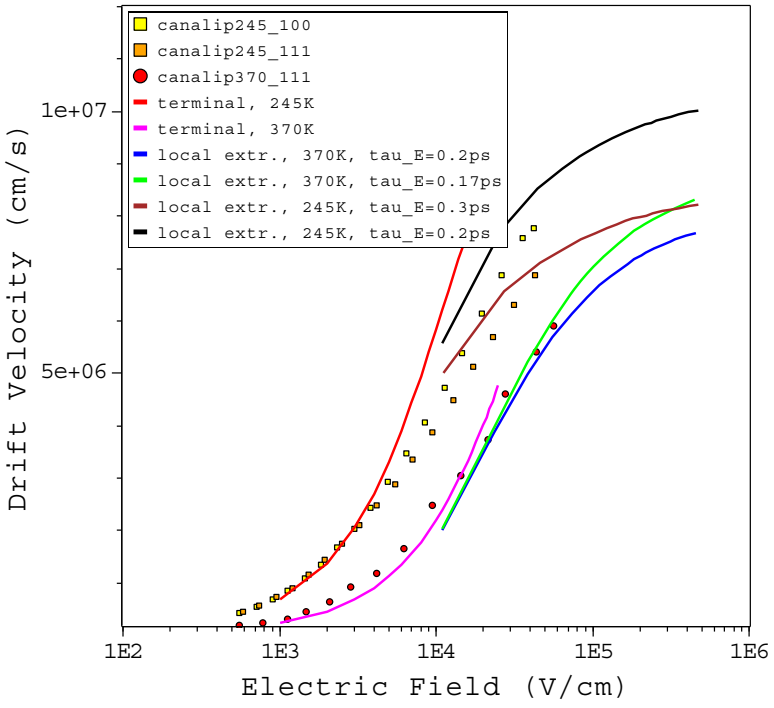

Figure 10: Hole drift velocity versus electric field for different lattice temperatures.

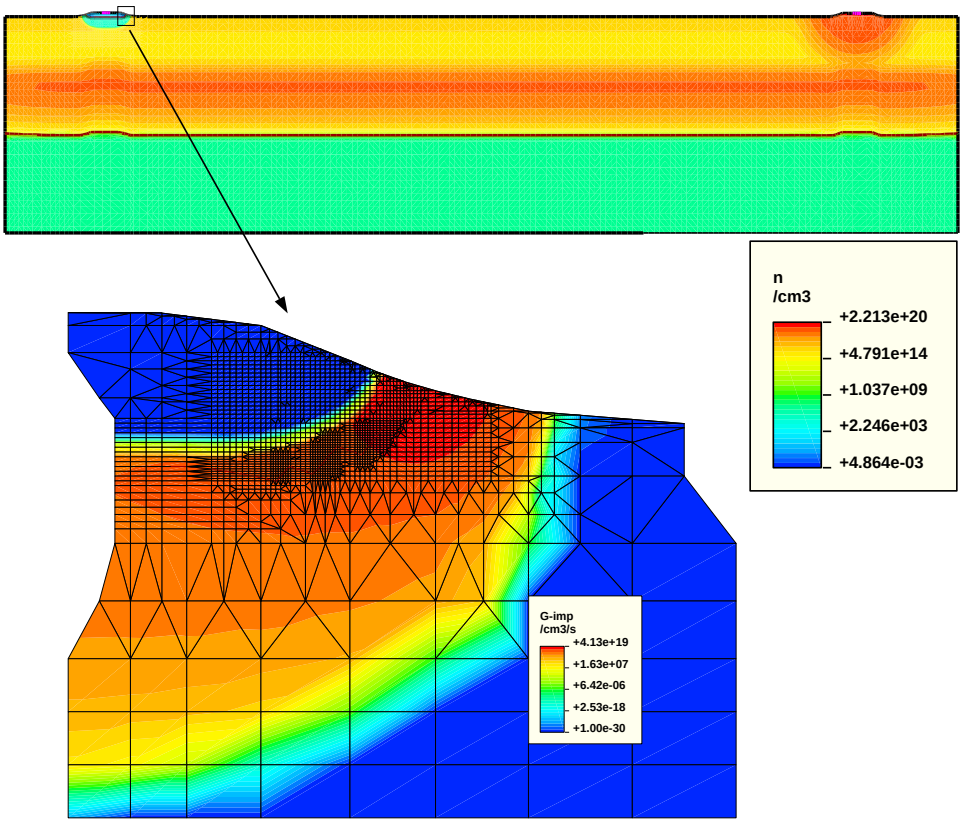

Figure 11: 2D cross section of the smart-power diode DIODE24_BL. The inset shows the distribution of the impact ionization rate at breakdown.

The maxima of the rate are located directly underneath the surface. The simulation of the breakdown voltage and the evaluation of the impact ionization model at high temperatures hence will be obscured by the uncertainty from the lateral doping profile *and* the possible existence of a surface channel for breakdown. In the following we *have to assume* that DIODE24_BL is nevertheless a suitable test device. Doping profile and electric field across the critical region are shown in Fig. 12. The field variation is about 20% over a distance of 100 nm which is smooth enough to justify the application of a local-field model.

The default simulation of the forward and reverse IV-characteristics is *defined* as follows: SRH (minority carrier) lifetimes independent on doping and temperature, fixed to $\tau_n = 1.4 \times 10^{-6}$ s, $\tau_p = 4.2 \times 10^{-7}$ s for the best fit to the SRH-dominated branch of the 298K forward IV-curve. Recombination processes are “Auger" (default parameters including the T-dependence of the Auger coefficients) and “SRH", BGN model is “slotboom", the statistics is “Boltzmann-Maxwell" (i.e. “Fermi" not switched on). Electron-hole scattering (“carrier-carrier", Brooks-Herring) has to be included for a correct curvature in the bias range -0.8 V – -1 V where plasma effects play an important role. Generation processes are “SRH" and impact ionization (“vanOverstraeten"). The critical fields in the Chynoweth law were lowered by 5% in order to match the measured breakdown voltage at 323 K: $b_n(low) =$

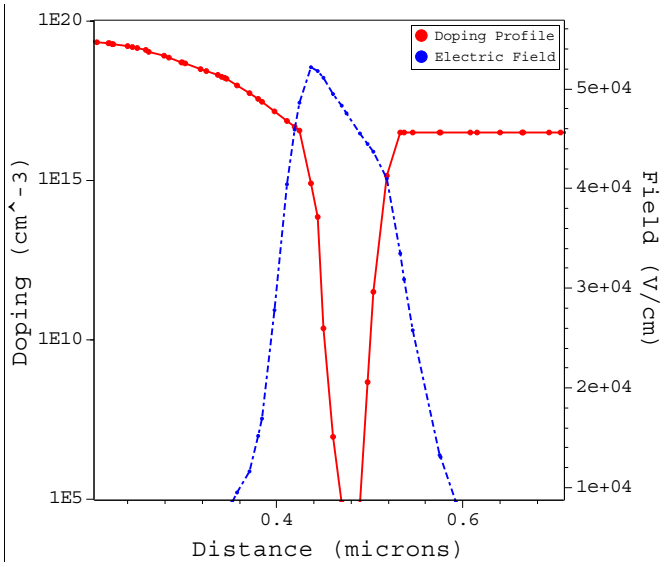

Figure 12: Doping concentration and electric field profile at zero bias across the p^+n junction near the surface.

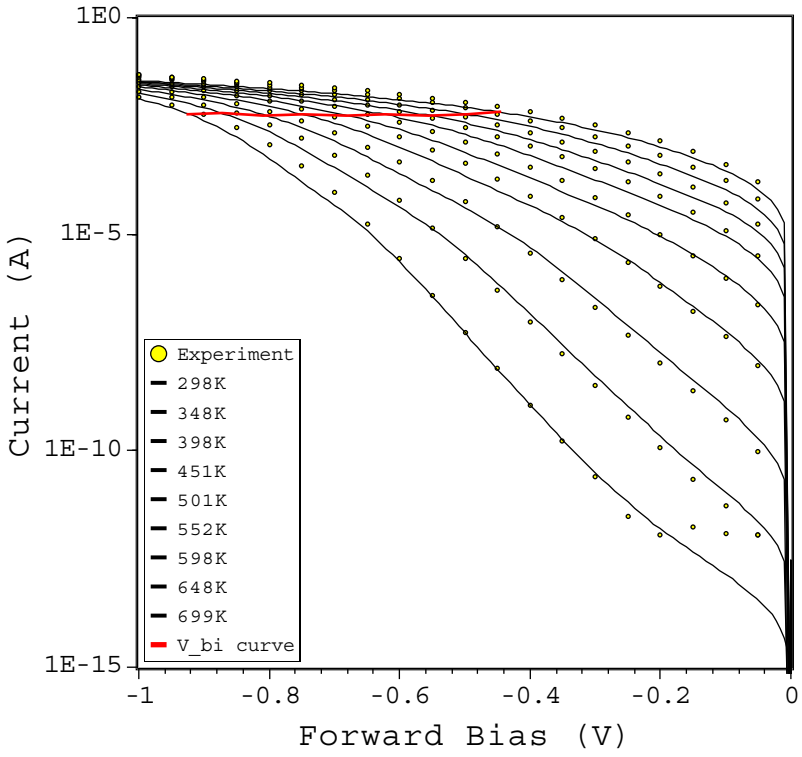

Figure 13: Default simulation and measured forward IV-characteristics. The horizontal red line connects the built-in potentials for each temperature.

1.1695×10^6 V/cm, $b_p(low) = 1.9342 \times 10^6$ V/cm, $b_n(high) = 1.1695 \times 10^6$ V/cm, $b_p(high) = 1.6083 \times 10^6$ V/cm. This can be considered as a concession to the above mentioned uncertainties induced by the lateral doping profile and the proximity of the surface. We *assume* that those effects, if present, have at the most a weak temperature dependence that can be neglected.

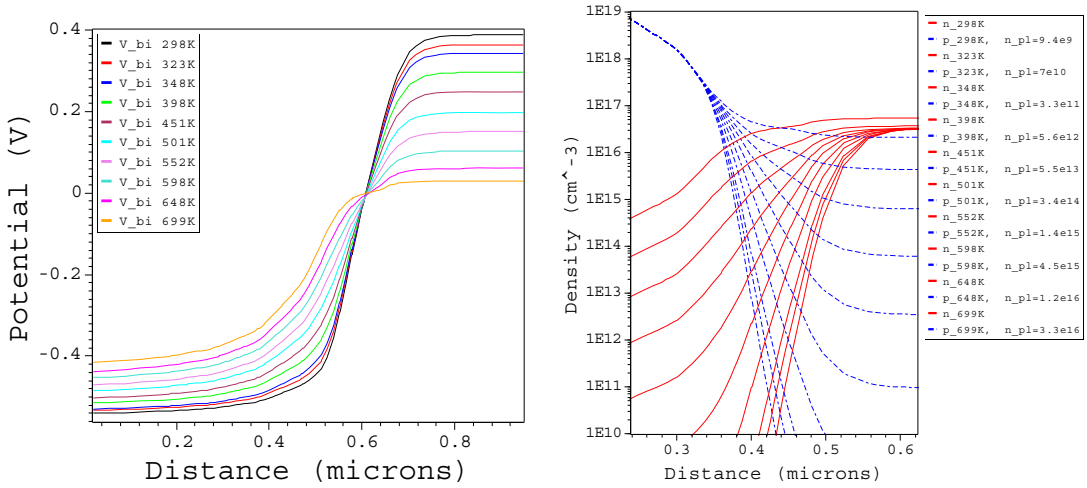

Figure 14: Built-in potential and free carrier densities in the depletion zone at zero bias. In the right legend n_{pl} denotes the extracted plasma density (n=p).

The forward and reverse IV-characteristics in the temperature range 298 K – 699 K are presented in Figs. 13 and 15, respectively. Since the intrinsic density of silicon at 700 K is about 3.36×10^{16} cm^{-3}, a main feature is the transition from the extrinsic to the intrinsic regime at some elevated temperature (depending on the local doping concentration). In the forward-bias range we observe that SRH recombination dominates up to a current of 1×10^{-5} A for *all* temperatures. Then some Auger process starts to dominate (either band-to-band (b2b) Auger or trap-assisted Auger (TAA)) which also defines the onset of a remarkable deviation of the simulated from the measured current. This deviation extends up to -1V and covers the entire bias range at the highest temperatures. SRH recombination is completely masked in the range 550 K – 700 K. Hence the forward-bias branch is not suitable to draw any conclusions about a temperature dependence of the SRH lifetimes.

The shrinkage of the built-in potential with increasing temperature is depicted in Fig. 14. If the built-in potential is marked on each corresponding curve in Fig. 13, one obtains an almost horizontal line. In Fig. 14 it is also shown how a plasma develops in the depletion zone with rising T (plasma density $n_{pl} = n = p$ equal to the intrinsic density n_i). One can see that above 600 K the electron density in the neutral n-region exceeds the doping, which results in the above-mentioned intrinsic behavior.

A first inspection of the reverse-bias characteristics in Fig. 15 shows two features: the strong overestimation of the SRH-dominated current between 323 K and 450 K, and far too large breakdown voltages for the higher temperatures. Below 1×10^{-11} A the experimental data turn into noise and are disregarded. A closer look on various quantities near breakdown at 323 K and 648 K, respectively, reveals some

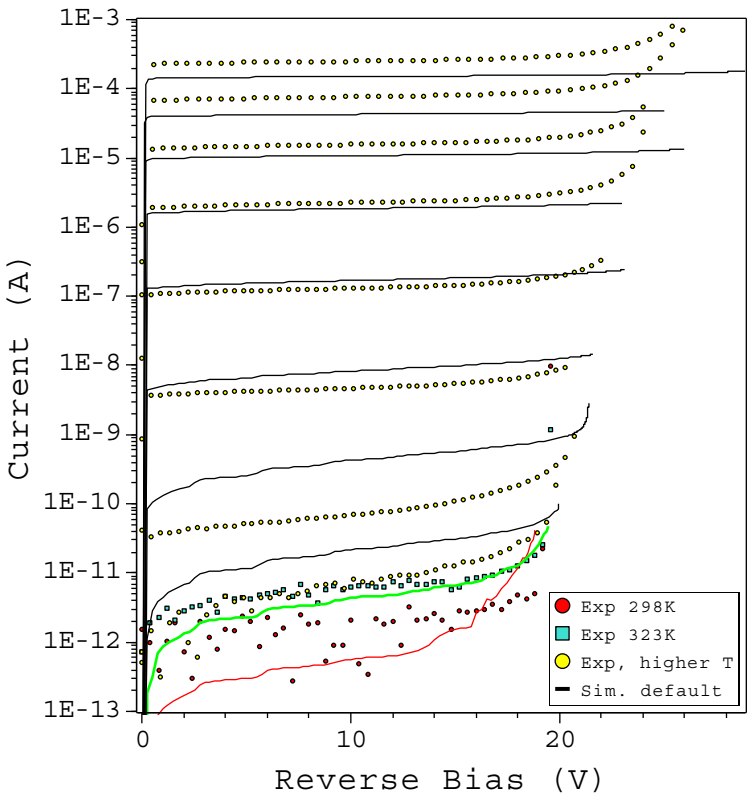

Figure 15: Default simulation and measured reverse IV-characteristics.

interesting aspects. In Fig. 16 electric field and ionization rate across the junction are compared for the two temperatures. Since the maxima of the field are not much different from each other, the exponential function in the Chynoweth law produces a factor 2 difference at the most. However, the ionization rates differ by more than four orders of magnitude (3.7×10^4)! This large difference is caused by the plasma density in the “depletion" region. (The impact ionization rate has the form $G^{II} = \alpha_n n v_n + \alpha_p p v_p$.) As indicated in the left part of Fig. 17, the plasma has a density of about $2.8 \times 10^{12}\,\mathrm{cm}^{-3}$ at 648 K, a factor of 6.2×10^4 larger than in the case of 323 K. On the other hand, this plasma density is much smaller than the intrinsic density at 648 K, which is about $1.2 \times 10^{16}\,\mathrm{cm}^{-3}$. As the temperature increases, the SRH rate extends into the *entire* n-region because n_i first *approaches* the electron density there, and finally it *determines* the electron density.

3.2 Forward-bias analysis

To understand the physics behind the forward IV-characteristics it is useful to plot the dominant recombination processes. In Figs. 18 and 19 we present the profiles of the Auger and SRH rates along a vertical cut through the device that also covers the buried layer (BL). These profiles are shown for the two limiting temperatures and for three forward biases. In the right part of the figures the integrated rates as a function

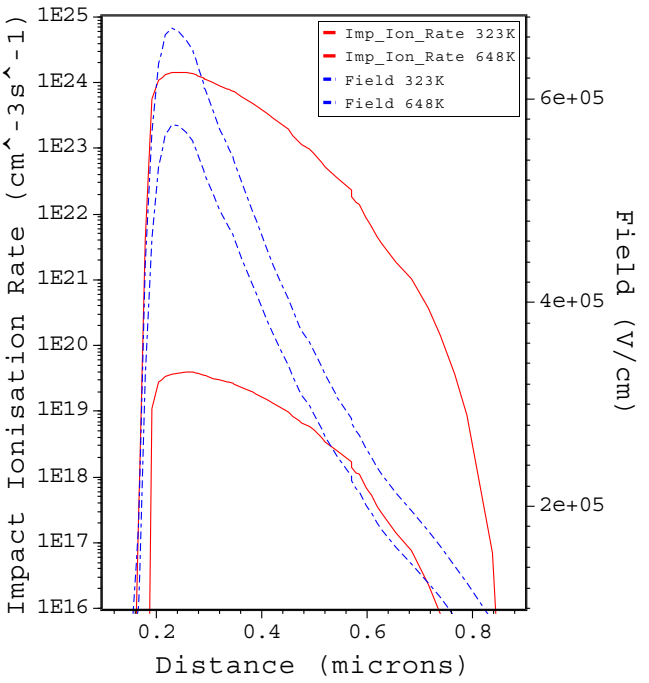

Figure 16: Electric field and impact ionization rate across the junction for two temperatures.

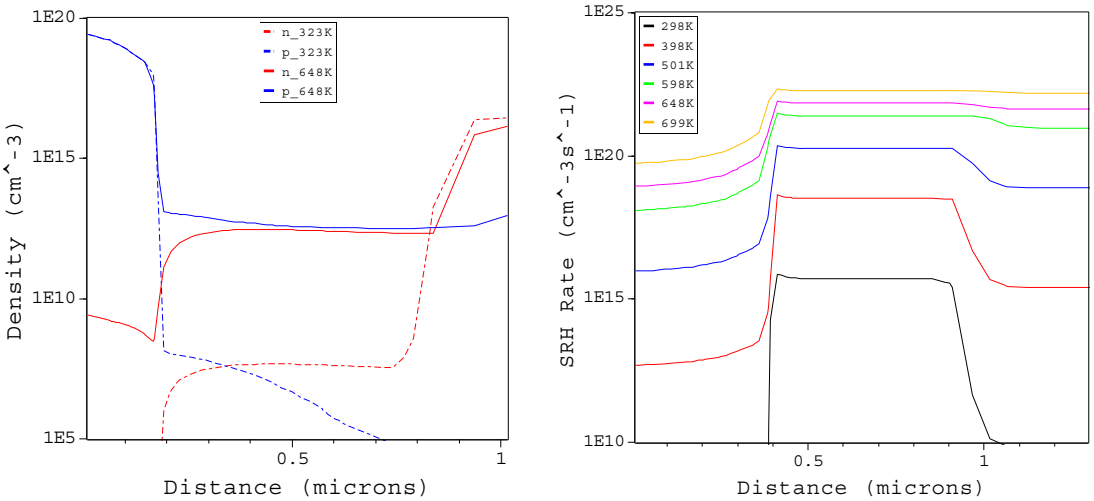

Figure 17: Free carrier densities at breakdown (left) and SRH rate at +12 V bias (right) across the junction for different temperatures.

of distance from the surface yield information about the relative contribution from different regions. At 298 K the Auger rates are concentrated in the p^+-region and the integrated Auger rate collects only very small contributions from the BL. The SRH

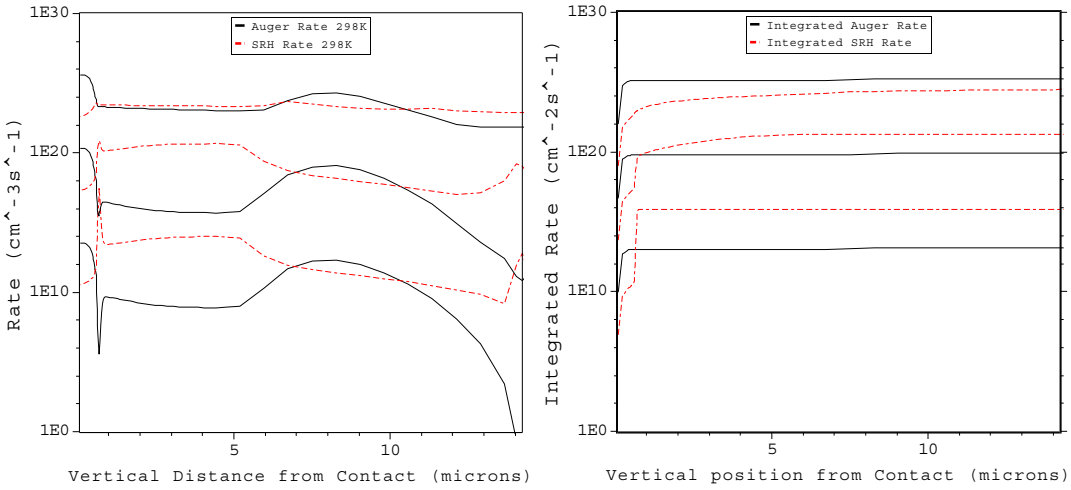

Figure 18: Profiles of the Auger and SRH rates at 298 K for V_{bias} = -0.2 V, -0.6 V, and -1.0 V from bottom to top (left). Integrated rates as a function of distance from the p-contact (right).

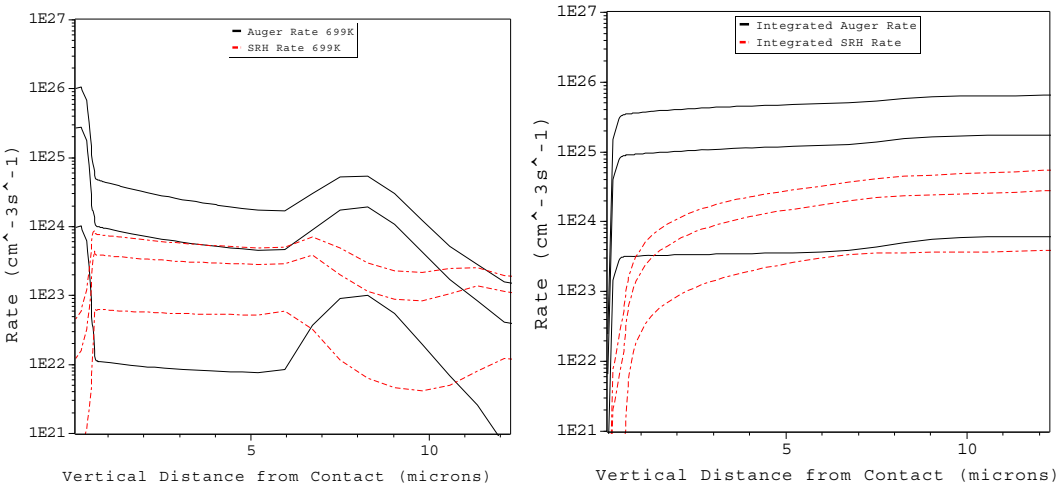

Figure 19: Profiles of the Auger and SRH rates at 699 K for V_{bias} = -0.2 V, -0.6 V, and -1.0 V from bottom to top (left). Integrated rates as a function of distance from the p-contact (right).

rate exhibits the usual peak in the depletion zone which disappears as the built-in voltage becomes zero. At high bias and high temperatures the SRH rate distribution is broad. SRH recombination is outnumbered by Auger recombination between -0.6 V and -1 V (from the IV-curve we find -0.66 V). At 699 K Auger recombination dominates in the whole forward bias range, but the BL region yields some contributions. This confirms the remarks made in the previous section. The transition from SRH to Auger dominance is easily seen from a plot of the ideality factor for all

temperatures in Fig. 20.

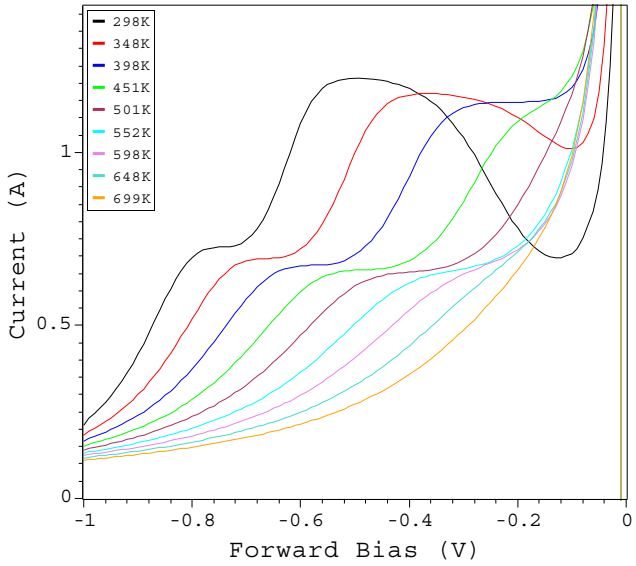

Figure 20: Ideality factor as function of ambient temperature.

We can draw the following important conclusion. Currents larger than 1×10^{-5} A originate from an Auger-type recombination process. At lower temperatures its rate is concentrated in the p^+-contact region. Hence for b2b Auger $R^{Auger} = C_{hhe}\, p^2 n$ there, and since n is fixed by N_A^-, a temperature effect can only be due to the minority carrier density n or/and the Auger coefficient C_{hhe}. Besides b2b Auger, a second recombination process is possible in this regime: trap-assisted Auger (TAA) recombination. TAA is a SRH-type recombination process where the energy difference between band edge and trap level is transfered to excited electrons/holes. TAA starts to exceed the thermal SRH rate when $c(n+p) \sim 1/\tau_{SRH}$, where c is the TAA coefficient in DESSIS$_{-\mathrm{ISE}}$. Then the TAA rate has a maximum in the p^+-contact region (like b2b Auger), but also a broad and large distribution in the *entire* n-region (like thermal SRH) giving the major contribution simply due to its large volume. In both regions the TAA rate turns into $R^{TAA} = c\, p\, n$!

In order to understand the shape of the forward IV-curves and their temperature dependence, we have to care about the following issues:

1.) The T-dependence of the band gap $E_g(T)$ as it influences n.
2.) The effect of the carrier statistics, since it affects the T-dependence of the quasi Fermi levels.
3.) The BGN model, since it determines the minority carrier densities.
4.) The size of C_{hhe}, C_{eeh} and the impact of their T- and n, p-dependence.
5.) The influence of surface recombination.
6.) The role of TAA and a possible T-dependence of c.

1.)
A striking misfit between measured and simulated forward IV-curves is the wrong

temperature dependence highlighted in Fig. 21. In order to check the influence of $E_g(T)$ the parameters in $E_g(T)$ were changed in such a way that the gap shrinkage was enhanced up to a reasonable limit guided by the experimental data in Fig. 1. The resulting effect was far too weak to explain the discrepancy in Fig. 21.

2.) and 3.)

The carrier statistics and different BGN models have a strong impact on the minority carrier density. Using any “traditional" BGN model in combination with Fermi statistics will give the same minority carrier density as without “Fermi" (a wanted feature in DESSIS$_{-\mathrm{ISE}}$). To force Fermi statistics without neglecting BGN at all, the "schenk" BGN was used [5]. Again, the distance between the 298 K and 699 K curves is not essentially changed.

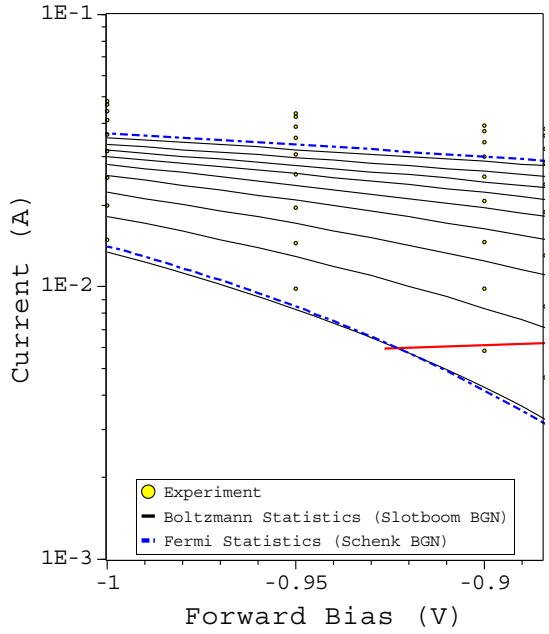

Figure 21: The effect of carrier statistics and different BGN models on the temperature dependence of the forward IV-characteristics.

4.)

The b2b Auger coefficients C_{hhe} and C_{eeh} were systematically increased neglecting their temperature dependence. As shown in Fig. 22 one can match the data points in the Auger-dominated range with values of the order $10^{-29} - 10^{-28}\,\mathrm{cm^6 s^{-1}}$. However, such values are 2 - 3 orders of magnitude larger than the usual and well-accepted value of $10^{-31}\,\mathrm{cm^6 s^{-1}}$.

5.)

The minority carrier density at the surface never exceeds $10^{16}\,\mathrm{cm^{-3}}$. Assuming $v_{surf} = 10^4$ cm/s for the surface recombination velocity, the resulting rate of surface recombination is always much less than the integrated rates shown in the right part of Figs. 18 and 19 (at small forward bias and for the lower temperatures the minority carrier density is very small). Therefore, surface recombination can be safely ignored.

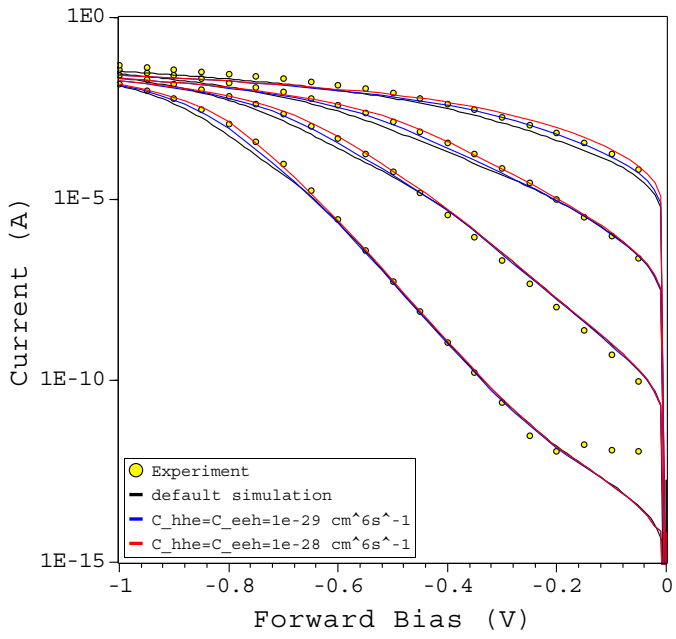

Figure 22: Variation of the b2b Auger coefficients (frozen T-dependence) for 298 K, 398 K, 501 K, and 648 K (from bottom to top).

6.)
The remaining thinkable process is TAA recombination [2], (p. 80). Results for $c = 1 \times 10^{-11}$ and $c = 5 \times 10^{-11}\,\mathrm{cm^3 s^{-1}}$ are presented in Fig. 23. Termination of simulated curves is caused by non-convergency of DESSIS$_{-\mathrm{ISE}}$. With $c = 5 \times 10^{-11}\,\mathrm{cm^3 s^{-1}}$ a good fit for all temperatures could be obtained. c might have a similar temperature dependence as the b2b Auger coefficients (thought to be due to phonon-assistance), although the spread of the deep-level wave functions in k-space would relax momentum conservation restrictions. Unfortunately, no assessment about the temperature dependence of c can be made.

That TAA recombination could be identified as the dominant recombination process is not surprising. The implantation of the BL both creates a large volume of high electron density in favor of an Auger process *and* a large density of deep-lying trap states in favor of a SRH process. Hence the device behavior under forward bias is practically determined by induced features from the BL.

3.3 Reverse-bias analysis

3.3.1 Lifetimes

The pre-breakdown branches of the reverse-bias curves exhibit a change from a rounded shape at “low" temperatures to an almost rectangular shape at higher temperatures. The temperature dependence itself seems to be irregular when compared with the default simulation. To gain more insight into the measured behavior we plot the SRH rate at +12.5 V along a vertical cross section through the device including

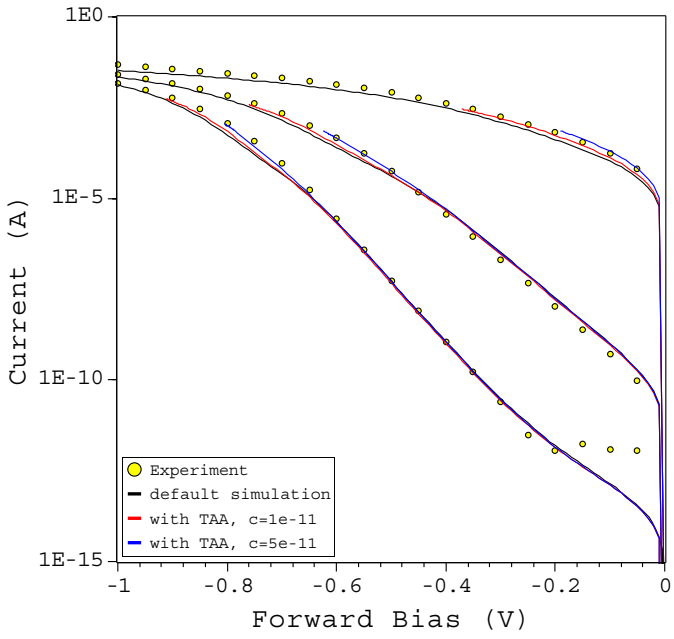

Figure 23: Variation of the TAA coefficient c for 298 K, 398 K, and 648 K (from bottom to top).

the BL region in Fig. 24. Note that the volume of the outer region is huge com-

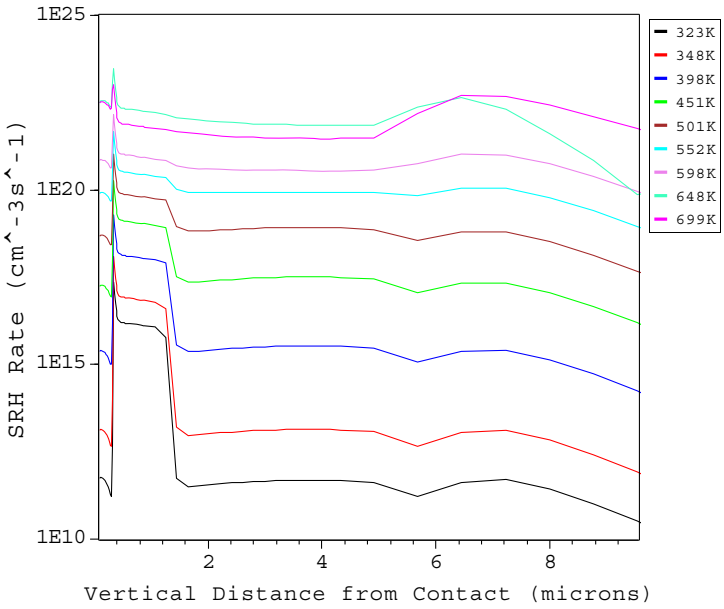

Figure 24: Profiles of the SRH rate at a bias of +12.5 V along a vertical cut through the device from the p^+-contact to the pn-junction of the BL for various temperatures. Lifetime parameters were the same as in the previous section.

pared to the volume of the p^+n depletion zone. At “low" temperatures the depleted p^+n-junction yields the major contributions, but at an intermediate temperature the outer region has a comparable share, whereas at the highest temperatures the BL part of the outer region dominates the SRH rate. This change in the relative contributions to the total SRH rate is essential to understand the reverse-bias IV-curves. The maximum doping in the BL is about $8 \times 10^{18}\,\mathrm{cm}^{-3}$, far more than in the depleted p^+n-junction. Since the minority carrier lifetimes are strongly affected by the process conditions, in particular by implantations with a high dose, heavily doped regions have (much) smaller lifetimes which is expressed by the so-called Scharfetter relation (SRH(DopingDependence) in DESSIS$_{-\mathrm{ISE}}$) [2], (p. 73). The blue curves in Figs. 26 and 27 were obtained with the default parameter set including “DopingDependence", i.e. the lifetime parameters “taumax" were set back to Dessis default. By chance, the agreement at 323 K is the same as before (compare Fig. 15). Applying the Scharfetter relation we obtain pictures as in Fig. 25 where the SRH rate (left) and the hole lifetime (right) are shown for the “intermediate" temperature of 348 K.

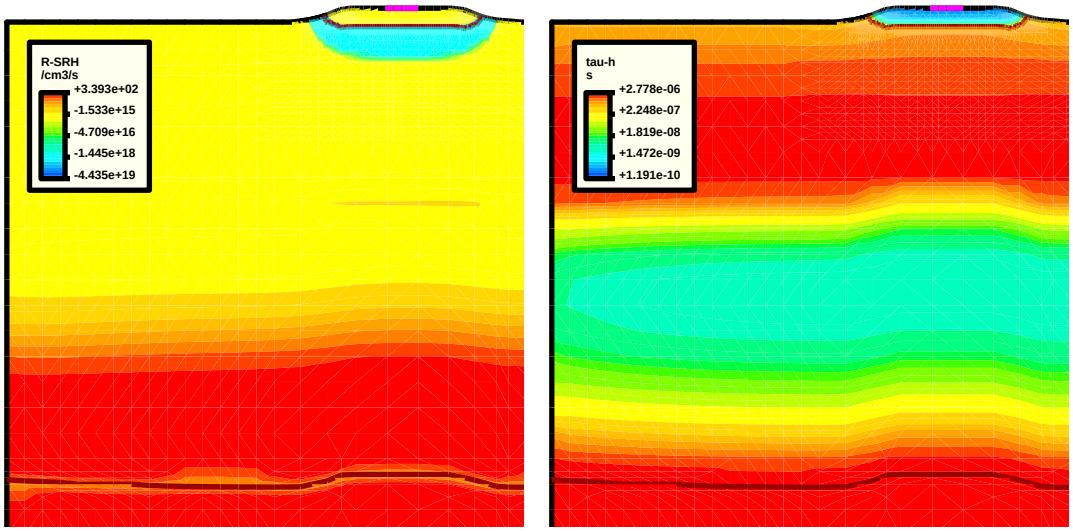

Figure 25: Distributions of the SRH rate (left) and of the hole lifetime (right) throughout the device.

One observes that the hole lifetime in the depletion zone of the p^+n-junction (blue region on the left side) is much larger (the color is orange!) than that in the BL region (green-blue area on the right side). Although the BL region is quasi-neutral, this leads to a total contribution to the SRH rate (yellow area on the left side) which is comparable to the contribution from the highly depleted p^+n-junction. The qualitative difference in the curve shape is caused by the different speed at which the SRH rates reach their full size when the reverse bias is turned on. Since in the BL region n is always much larger than n_1, the rate turns into $R^{SRH} = [N_D^{(BL)}\,p - n_{i,eff}^2]/(\tau_p^{(BL)}\,N_D^{(BL)})$ there. p decreases everywhere in the BL, but the denominator remains constant. In the p^+n-junction we have $R^{SRH} = [n\,p - n_{i,eff}^2]/[\tau_p^{(pn)}\,(n+n_1) + \tau_n^{(pn)}\,(p+p_1)]$. $n\,p$ in the numerator decreases, but also n and p in the denominator, i.e. it takes longer

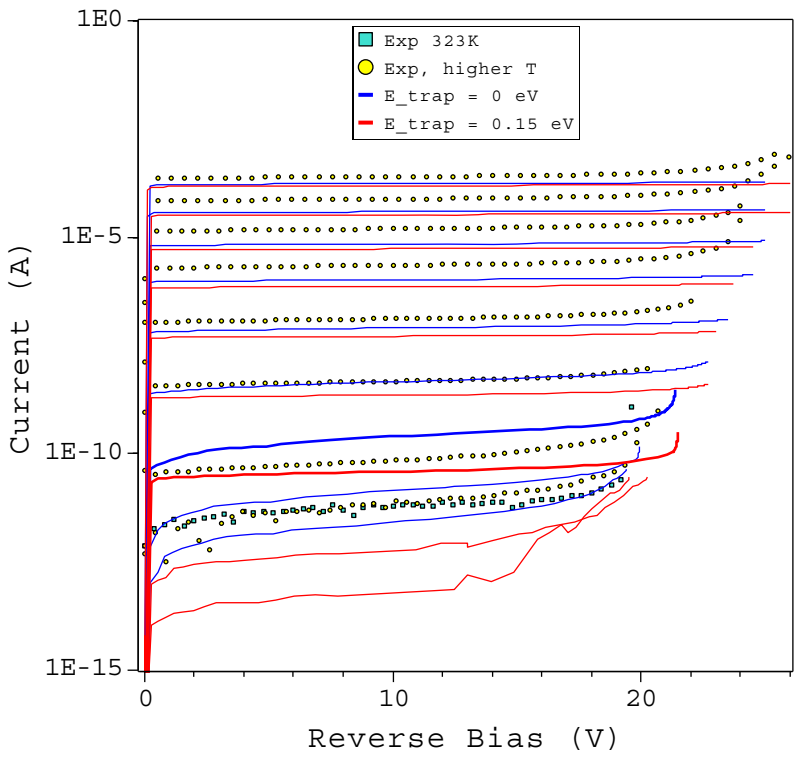

Figure 26: Reverse-bias IV-curves with default lifetime parameters including “DopingDependence" in SRH (blue solid lines) and with $E_{trap} = 0.15$ eV (red solid lines).

to “switch on" the rate to its (large) maximum level in the p^+n-junction.

Comparison of the 398 K default simulation with the measured data (the blue bold line in Fig. 26) reveals that the transition to the BL-dominated generation has already occurred at this temperature in reality, but not in the simulation. One can easily increase the relative contribution of the BL region e.g. by shifting the trap level out of its mid gap position. In Fig. 26 we used $E_{trap} = 0.15$ eV which increases $n_1 = n_{i,eff} \exp(E_{trap}/k_B T)$ and, therefore, decreases R^{SRH} in the p^+n-junction but not much in the BL region. The resulting IV-curves are shown in red in Fig. 26. At 398 K the shape of the curve is now more rectangular and fits better the measured shape.

On the other hand, one can play with the parameters of the Scharfetter relation to increase the importance of one particular region and, at the same time, to increase or decrease the total SRH rate. A perfect fit is not attainable because it would require the knowledge of the different lifetime profiles in the p^+n-junction and the whole outer region, respectively. Fig. 27 shows the result if the power “*alpha*" in the Scharfetter relation is increased from 1 to 1.5 (red solid lines). Now all curves are shifted up giving a reasonable agreement between 450 K and 700 K. From these exercises we draw the conclusion that also the reverse-bias branch does not yield information about the temperature dependence of the minority carrier lifetimes. Note, that the lifetime parameters “*taumax*" were not changed at all so far. For the fol-

lowing analysis of the breakdown voltages at different temperatures we used the parameters "$alpha$" $= 1.5$ (electrons and holes), "$taumax$" $= 1 \times 10^{-6}$ s (electrons), "$taumax$" $= 1 \times 10^{-5}$ s (holes), and $E_{trap} = 0.1$ eV. The remaining lifetime parameters were default. With this choice a reasonable over-all agreement is found (the blue solid lines in Fig. 28).

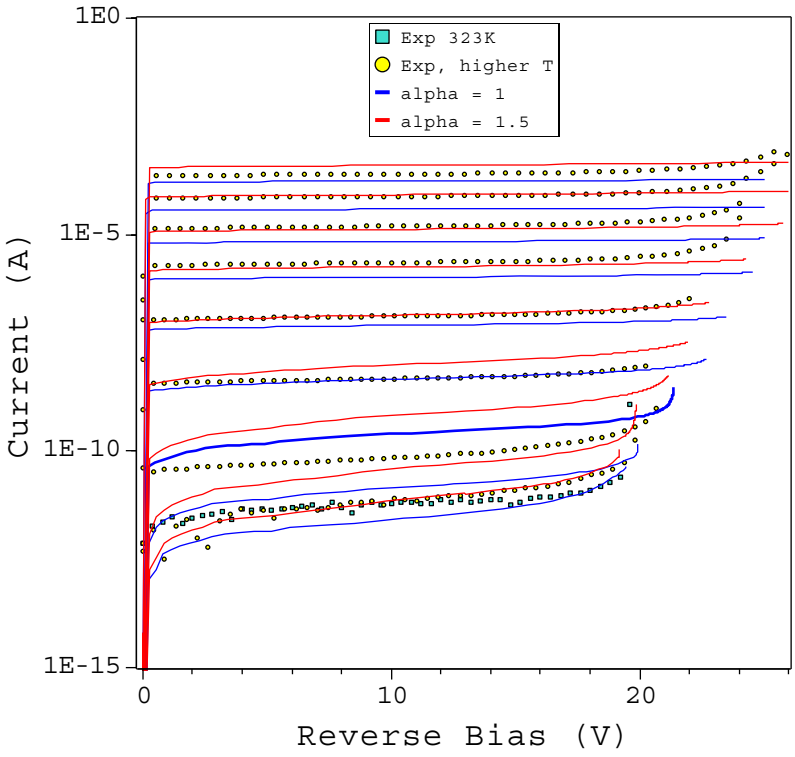

Figure 27: Reverse-bias IV-curves with default lifetime parameters including "DopingDependence" in SRH (blue solid lines) and with "$alpha$" $= 1.5$ (red solid lines).

3.3.2 Impact Ionization and Breakdown Voltages

Based on the analysis of the previous subsection we now turn to the avalanche breakdown. As already mentioned in Subsection 3.1, the huge difference between the impact ionization (II) rates at the temperature extremes does not arise from the electric field (which is comparable at breakdown) but from the difference of the plasma densities in the "depletion" region. The increasing plasma with temperature is probably the combined result of the high intrinsic density (which is not completely removed by the reverse bias) and the generated stationary carrier density (by II and SRH).

The Chynoweth form of the impact ionization coefficient $\alpha_{n,p} = \alpha_\infty \exp(-b_{n,p}/F)$ contains the ionization threshold energy E_i in both the exponent and the pre-factor: $b_{n,p} = E_i/(q l_{n,p})$, $\alpha_\infty = qF/E_i$ with the mean free paths for optical phonon scattering $l_{n,p}$. Since the ionization threshold is given by, or at least closely related to the indirect band gap, it is reasonable to assume that E_i has the

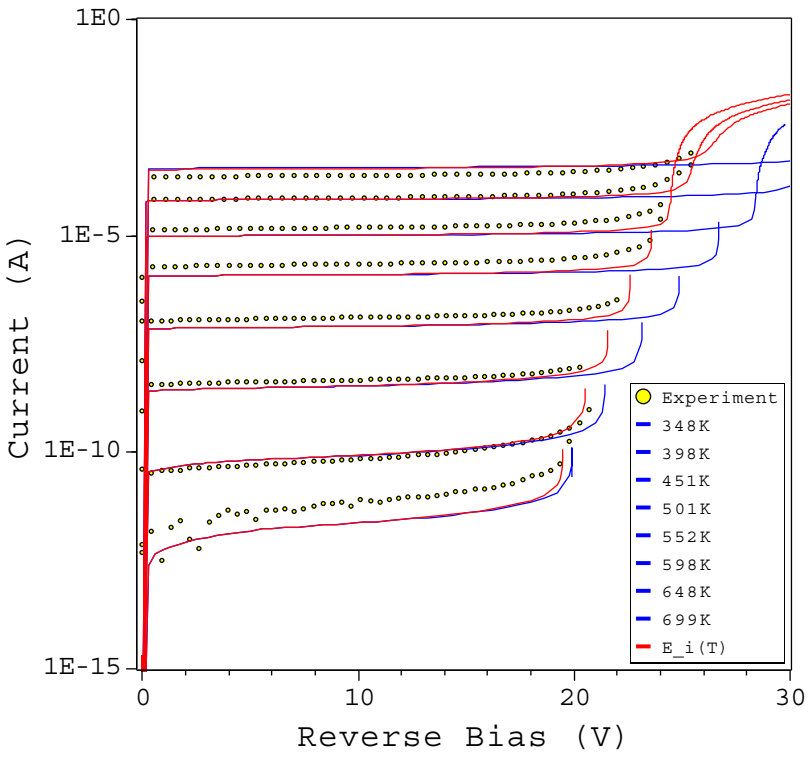

Figure 28: Reverse-bias IV-curves with optimized lifetime parameters. Blue solid lines: impact ionization rate as defined in the default simulation, red solid lines: with temperature dependent threshold energy $E_i(T)$ as described in the text.

same temperature dependence as E_g. (For the critical fields $b_{n,p}$ this can be already found e.g. in MEDICI.) The modification

$$\alpha = const\,\gamma \frac{E_g(300\,K)}{E_g(T)} \exp\left[-\frac{\gamma b}{F}\frac{E_g(T)}{E_g(300\,K)}\right]$$

was implemented in DESSIS$_{-\mathrm{ISE}}$ by A. Wettstein and can be used (at IIS) in the “vanOverstraeten" model with “Recombination (Avalanche (vanOverstraeten BandGap))". No BGN is possible and “NewDiscretization" has to be switched on.

Using this model, an excellent fit of the measured threshold voltages can be obtained as shown in Fig. 28. The saturation after the first breakdown is also clearly seen for the highest temperatures where the simulator converged up to 30 V. The good agreement proves that the modified avalanche model is reasonable and that the T-dependence of E_g is well modeled in DESSIS$_{-\mathrm{ISE}}$. On the other hand, the measured breakdown turns out to be softer than the simulated one. We checked whether trap-assisted tunneling can account for this. However, since only at the lowest temperatures the p^+n-junction dominates the SRH rate, the uppermost curves are not at all affected by trap-assisted tunneling. (The electric field in the BL region is negligible.) One can only argue that the above mentioned uncertainties (2D doping profile, proximity of the surface) are responsible for the weaker breakdown.

Acknowledgement

I'm grateful to Andreas Wettstein who implemented modifications of the mobility and avalanche models into the DESSIS$_{-\mathrm{ISE}}$ source code, and to Marina Valdinoci (University of Bologna) for the process simulation files of DIODE24_BL from MOD_B_BOSCH.

References

[1] A. Schenk, "Unified Bulk Mobility for Low- and High-Field Transport in Silicon," *J. Appl. Phys.*, vol. 79, no. 2, pp. 814–34, 1996.

[2] A. Schenk, *Advanced Physical Models for Silicon Device Simulation*. Computational Microelectronics, New York: Springer-Verlag, 1998.

[3] C. Canali, G. Majni, R. Minder, and G. Ottaviani, "Electron and Hole Drift Velocity Measurements in Silicon and their Empirical Relation to Electric Field and Temperature," *IEEE Trans. Electron Devices*, vol. ED-22, pp. 1045–47, 1975.

[4] P. M. Smith and J. Frey, "High-field Transport of Holes in Silicon," *Appl. Phys. Lett.*, vol. 39, pp. 332–33, 1981.

[5] A. Schenk, "Finite-Temperature Full-Random Phase Approximation Model of Band Gap Narrowing for Silicon Device Simulation," *J. Appl. Phys.*, vol. 84, no. 7, pp. 2296–2301, 1998.